Journal of Alloys and Compounds 509 (2011) 294–300

Contents lists available at ScienceDirect

Journal of Alloys and Compounds

journal homepage: www.elsevier.com/locate/jallcom

Hydrogen storage characteristics of nanocrystalline and amorphous Mg_2Ni-type alloys prepared by melt spinning

Yang-huan Zhang[a,b,*], Feng Hu[a,b], Zhi-gang Li[a,b], Ke Lü[a,b], Shi-hai Guo[b], Xin-lin Wang[b]

[a] School of Material, Inner Mongolia University of Science and Technology, Baotou 014010, China
[b] Department of Functional Material Research, Central Iron and Steel Research Institute, Beijing 100081, China

ARTICLE INFO

Article history:
Received 19 May 2010
Received in revised form 30 August 2010
Accepted 2 September 2010
Available online 21 September 2010

Keywords:
Mg_2Ni-type alloy
Mn substitution
Melt spinning
Hydrogen storage characteristics

ABSTRACT

In order to improve the hydrogen storage characteristics of the Mg_2Ni-type alloys, Ni in the alloy is partially substituted by element Mn, and melt-spinning technology is used for the preparation of the $Mg_2Ni_{1-x}Mn_x$ ($x = 0, 0.1, 0.2, 0.3, 0.4$) hydrogen storage alloys. The microstructures of the as-cast and spun alloys are characterized by XRD, SEM and HRTEM. The hydrogen absorption and desorption kinetics of the alloys are measured by an automatically controlled Sieverts apparatus. The electrochemical performances are tested by an automatic galvanostatic system. The results show that the as-spun Mn-free alloy holds typical nanocrystalline structure, whereas the as-spun alloys containing Mn displays a nanocrystalline and amorphous structure. The hydrogen absorption and desorption capacities and kinetics of the alloys increase with rising spinning rate. Additionally, melt spinning markedly improves the electrochemical hydrogen storage capacity and cycle stability of the alloys containing Mn. With an increase in the spinning rate from 0 (As-casts is defined as spinning rate of 0 m/s) to 30 m/s, the discharge capacity of the ($x = 0.3$) alloy mounts up from 92.3 to 211.1 mAh/g, and its capacity retaining rate at 20th charging and discharging cycle grows from 36.21% to 76.02%.

1. Introduction

Mg and Mg-based intermetallic compounds are intensively studied because they are considered as potential materials for solid state hydrogen storage in the form of metallic hydrides such as MgH_2 and Mg_2NiH_4. The theoretical hydrogen storage capacities of MgH_2 and Mg_2NiH_4 are 7.6 wt.% and 3.6 wt.% [1,2] respectively, which is quite adequate for commercial applications as a hydrogen fuel source [3]. However, their practical application to hydrogen suppliers has been limited mainly due to their sluggish hydriding/dehydriding kinetics as well as high thermodynamic stability of their corresponding hydride. To achieve the application goal, a variety of approaches, involving mechanical alloying (MA) [4], melt spinning [5], GPa hydrogen pressure method [6], hydriding combustion synthesis [7], surface modification [8], alloying with other elements [9], adding catalysts [10] etc., have been developed to overcome these drawbacks. Analysis of recent publications shows that the researches in this area have achieved prominent progress in hydrogen absorption/desorption kinetics of Mg-based alloys. However, thermodynamic stability and decomposition temperature of Mg-based hydrides are still too high for their practical utilization as hydrogen accumulators. Therefore, the scientists in this field still continue their attempts towards decreasing thermal stability of the Mg-based hydride.

Particularly, high-energy ball milling, a quite powerful method for the preparation of nanocrystalline and amorphous Mg and Mg-based alloys, is quite suitable to solubilize particular elements into MgH_2 or Mg_2NiH_4 above the thermodynamic equilibrium limit, which may facilitate to destabilize MgH_2 or Mg_2NiH_4 [11]. However, the milled Mg and Mg-based alloys show extremely poor hydrogen absorbing and desorbing cycle stability due to the fact that the metastable structures produced by ball milling tended to vanish during multiple hydrogen absorbing and desorbing cycles [12], which is an insurmountable bottleneck for their practical applications.

Alternatively, melt-spun technique can overcome the above-mentioned shortcoming and effective restraining the rapid degradation of hydrogen absorbing and desorbing cycle properties of Mg and Mg-based [13,14]. Furthermore, the melt-spinning technique is also an impactful method to obtain a nanocrystalline structure and is very appropriate for mass-production of nanocrystalline Mg-based alloys. Many literatures have clarified that nanocrystalline alloys produced by melt spinning could have excellent hydriding characteristics even at room temperature, similar to the alloys produced by the MA process. Spassov and Köster [15] prepared $Mg_2(Ni,Y)$ hydrogen storage alloy with precise

* Corresponding author at: Department of Functional Material Research, Central Iron and Steel Research Institute, 76 Xueyuan Nan Road, Haidian District, 100081 Beijing, PR China. Tel.: +86 010 62187570; fax: +86 010 62182296.
E-mail address: zyh59@yahoo.com.cn (Y.-h. Zhang).

0925-8388/$ – see front matter © 2010 Elsevier B.V. All rights reserved.
doi:10.1016/j.jallcom.2010.09.007

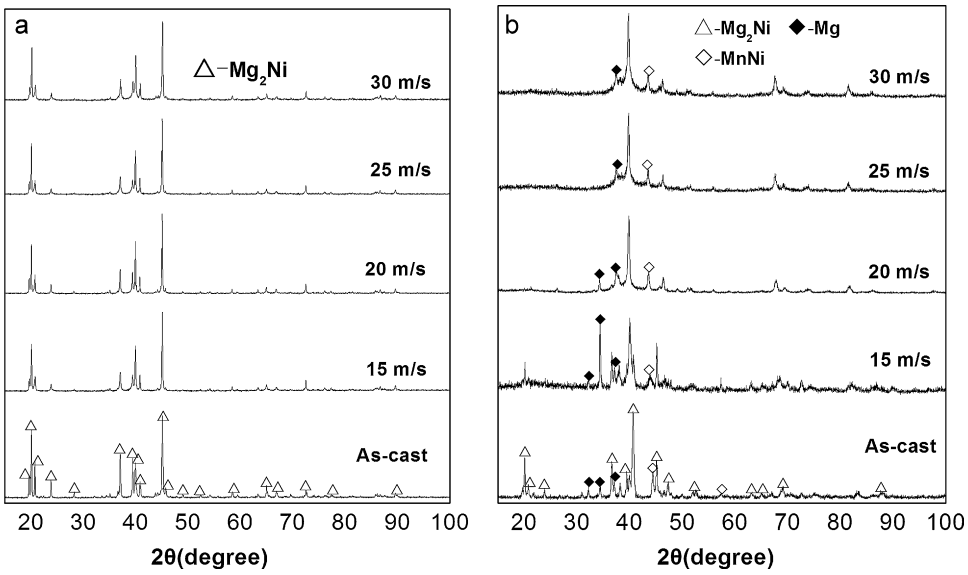

Fig. 1. XRD profiles of the as-cast and spun alloys: (a) Mn_0 alloy, (b) $Mn_{0.3}$ alloy.

composition $Mg_{63}Ni_{30}Y_7$ by melt spinning, and its maximum hydrogen absorption capacity (about 3.0 wt.%) and hydrogenation kinetics of the melt-spun $Mg_2(Ni,Y)$ were found to be comparable to the hydrogen absorption characteristics of nanocrystalline ball-milled Mg_2Ni and to exceed those of the conventionally prepared polycrystalline Mg_2Ni alloys. Huang et al. [16] prepared amorphous and nanocrystalline Mg-based alloy $(Mg_{60}Ni_{25})_{90}Nd_{10}$ by melt spinning, obtaining the highest discharge capacity of 580 mAh/g and the maximum hydrogen capacity of 4.2 wt.% H.

In this paper, the element Ni in Mg_2Ni alloy was partially substituted by Mn in order to enhance the glass forming ability of the Mg_2Ni-type alloys. The nanocrystalline and amorphous Mg_2Ni-type $Mg_2Ni_{1-x}Mn_x$ (x = 0–0.4) alloys are prepared by melt-spinning technique. Moreover, the influences of melt spinning on hydrogen storage performances of the alloys are examined in detail.

2. Experimental

The alloy ingots were prepared using a vacuum induction furnace in a helium atmosphere at a pressure of 0.04 MPa in order to prevent the volatilization of Mg during melting. A part of the as-cast alloys was re-melted and spun by melt spinning with a rotating copper roller. The spinning rate was approximately expressed by the linear velocity of the copper roller because it is too difficult to measure a real spinning rate i.e. cooling rate of the sample during spinning. The spinning rates used in the experiment were 15, 20, 25 and 30 m/s, respectively. The nominal compositions of the experimental alloys are $Mg_2Ni_{1-x}Mn_x$ (x = 0, 0.1, 0.2, 0.3, 0.4). For convenience, the alloys were denoted with Mn content as Mn_0, $Mn_{0.1}$, $Mn_{0.2}$, $Mn_{0.3}$ and $Mn_{0.4}$, respectively.

The phase structures of the as-cast and spun alloys were determined by X-ray diffraction (XRD) (D/max/2400). The diffraction, with the experimental parameters of 160 mA, 40 kV and 10°/min respectively, was performed with $CuK_{\alpha 1}$ radiation filtered by graphite. The effective crystal sizes were calculated from Scherrer's formula.

The thin film samples of the as-spun alloys were prepared by ion etching method for observing the morphology with high-resolution transmission electron microscope (HRTEM) (JEM-2100F, operated at 200 kV), and for determining the crystalline state of the samples with electron diffraction (ED). The average grain sizes of the as-spun alloys were measured by linear intercept method on HRTEM micrographs.

The alloy ribbons were pulverized into fine powder of about 20 μm in sizes by mechanical milling and then mixed with carbonyl nickel powder in a weight ratio of 1:4. The mixture was cold pressed at a pressure of 35 MPa into round electrode pellets of 10 mm in diameter and total mass of about 1 g. The electrochemical characteristics of the experimental alloy electrodes was tested by a tri-electrode open cell, consisting of a metal hydride electrode, a sintered $NiOOH/Ni(OH)_2$ counter electrode and a Hg/HgO reference electrode. The electrolyte is a solution of 6 M KOH. The voltage between the negative electrode and the reference electrode was defined as the discharge voltage. In every cycle, the alloy electrode was first charged at a constant current density, and following the resting for 15 min, it was discharged at the same current density to −0.500 V cut-off voltage. The environment temperature of the measurement was kept at 30 °C.

The hydrogen absorption and desorption kinetics of the alloys were measured by an automatically controlled Sieverts apparatus. The hydrogen absorption was conducted at 1.5 MPa and the hydrogen desorption in a vacuum (1×10^{-4} MPa) at 200 °C.

3. Results and discussion

3.1. Structure characteristics

Shown in Fig. 1 are the XRD patterns of the Mn_0 and $Mn_{0.3}$ alloys, indicating that that there is no detectable amorphous phase in the as-spun Mn_0 alloy, but the as-spun $Mn_{0.3}$ alloy clearly shows the presence of an amorphous phase. Therefore, it can be concluded that the substitution of Mn for Ni facilitates the glass formation in the Mg_2Ni-type alloy. Two possibilities can be considered as the reasons for Mn substitution enhancing the glass forming ability of Mg_2Ni-type alloy. Firstly, the addition of third element to Mg-Ni or Mg–Cu alloys can significantly facilitate the glass formation [17,18]. Secondary, atomic radius of Mn is larger than Ni due to the fact that the glass forming ability of the alloy is closely relevant to the difference of the atomic radius of the components of the alloy. The bigger the difference of the atom radius, the higher the glass forming ability of the alloy is [19]. A comparison of Fig. 1(a) with (b) indicates that the substitution of Mn for Ni, instead of changing the major phase in the alloy, leads to the formation of Mg and MnNi phases. Listed in Table 1 are the lattice parameters, cell volume and full width at half maximum (FWHM) values of the main diffraction peaks of the as-cast and spun Mn_0 and $Mn_{0.3}$ alloys which were calculated by Jade 6.0 software. It can be seen from Table 1 that the melt spinning causes a visible increase in the FWHM values of the main diffraction peaks of the alloys, to be doubtless attributed to the refined grains and the stored stress in the grains produced by the melt spinning. Based on the FWHM values of the broad diffraction peak (2 0 3) in Fig. 1, the crystalline sizes $\langle D_{hkl} \rangle$ (nm) of the as-spun alloy are calculated using Scherrer's equation. The grain sizes of the as-spun alloys are in a range of 3–8 nm, basically consistent with results reported by Friedlmeier et al. [20]. It can also be derived from Table 1 that the substitution of Mn for Ni causes an evident increase in the FWHM values of the main diffraction peaks and a notable enlargement in lattice parameters and cell volume of the as-cast and spun alloys, to be attributed to the radius of Mn atom being larger than Ni atom.

Table 1
Lattice parameters, cell volume and FWHM values of the major diffraction peaks of the alloys.

Spinning rate (m/s)	FWHM values				Lattice parameters and cell volume					
	2θ (20.02°)		2θ (45.14°)		a (nm)		c (nm)		V (nm^3)	
	Mn_0	$Mn_{0.3}$	Mn_0	$Mn_{0.3}$	Mn_0	$Mn_{0.3}$	Mn_0	$Mn_{0.3}$	Mn_0	$Mn_{0.3}$
0	0.122	0.183	0.169	0.332	0.5210	0.5217	1.3244	1.3301	0.3112	0.3135
15	0.125	–	0.171	0.500	0.5210	0.5221	1.3251	1.3310	0.3115	0.3141
20	0.129	–	0.173	–	0.5210	0.5221	1.3258	1.3319	0.3117	0.3144
25	0.131	–	0.179	–	0.5211	0.5222	1.3265	1.3323	0.3119	0.3144
30	0.133	–	0.182	–	0.5211	0.5222	1.3287	1.3332	0.3124	0.3148

As the XRD analysis, a multiphase structure in the as-spun alloy is detected by HRTEM. A grey block (denoted as A) and a white block with a regular polygon morphology (denoted as B) can be seen in Fig. 2, which are determined to be MnNi and Mg phases by EDS analysis.

Illustrated in Fig. 3 are the HRTEM micrographs and electron diffraction (ED) patterns of the as-spun $Mn_{0.3}$ alloy. It is evident that the amorphization degree of the alloys visibly rises with increasing the spinning rate. The as-spun (15 m/s) $Mn_{0.3}$ alloy exhibits a nanocrystalline microstructure with an average grain size of about 8 nm, and its ED pattern appears sharp multi-haloes, corresponding to a crystal structure. With increasing the spinning rate, the morphologies of the as-spun $Mn_{0.3}$ alloy display a distinct feature of the nanocrystalline embedded in the amorphous matrix, and their ED rings consist of broad and dull halo, confirming the presence of an amorphous structure, which agrees very well with the XRD observation shown in Fig. 1.

3.2. Electrochemical hydrogen storage performances

3.2.1. Activation capability and discharge capacity

Electrochemical galvanostatic charge/discharge is a more effective and less time-consuming method for determining the absorbing hydrogen capacity than a gaseous technique. The cycle number dependence of the discharge capacity of the Mn_0 and $Mn_{0.3}$ alloys was illustrated in Fig. 4, at a charging–discharging current density of 20 mA/g. The figure shows that all the alloys have excellent activation performances, attaining their maximum discharge capacities at first charging–discharging cycle. The melt spinning inflicts an imperceptible impact on the activation performances of the alloys. The evolution of the maximum discharge capacities of the alloys with the spinning rate is shown in Fig. 5, indicating that the melt spinning clearly enhances the discharge capacity of the alloys. As the spinning rate grows from 0 (As-casts is defined as spinning rate of 0 m/s) to 30 m/s, the maximum discharge capacity increases from 30.3 to 116.7 mAh/g for the Mn_0 alloy, and from 92.3 to 211.1 mAh/g for the $Mn_{0.3}$ alloy. Some explanations may be offered as the reason of which leads to above-mentioned results. The observed essential differences in the discharge capacity of the alloys caused by the melt spinning most probably have to be associated with the differences in their microstructures. The crystalline material, when melt spun, becomes at least partially disordered and its structure changes to nanocrystalline or amorphous. Thus, high densities of crystal defects are introduced. Additionally, as a result of the defects introducing distortion of crystal lattice, the stored sufficient energy as chemical disorder and the introduced defects will produce internal strain. It was concluded by Niu and Northwood [21] that the exchange current density and H-diffusion coefficient

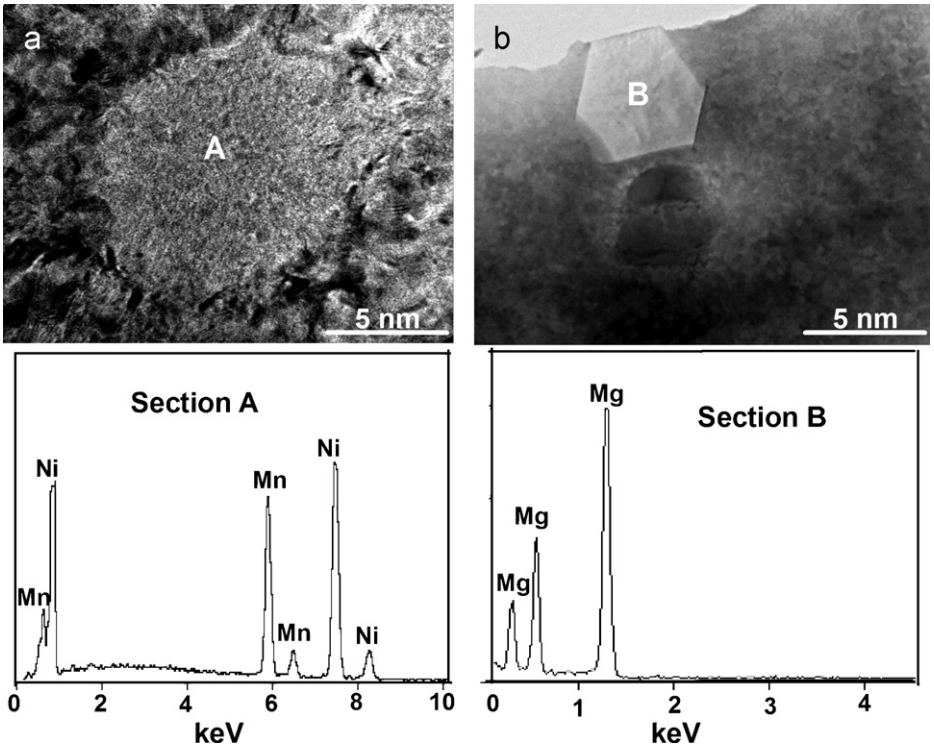

Fig. 2. HRTEM observation of Mg and MnNi phases in the as-spun (30 m/s) $Mn_{0.4}$ alloy together with typical EDS patterns of sections A and B in (a) and (b): (a) MnNi phase, (b) Mg phase.

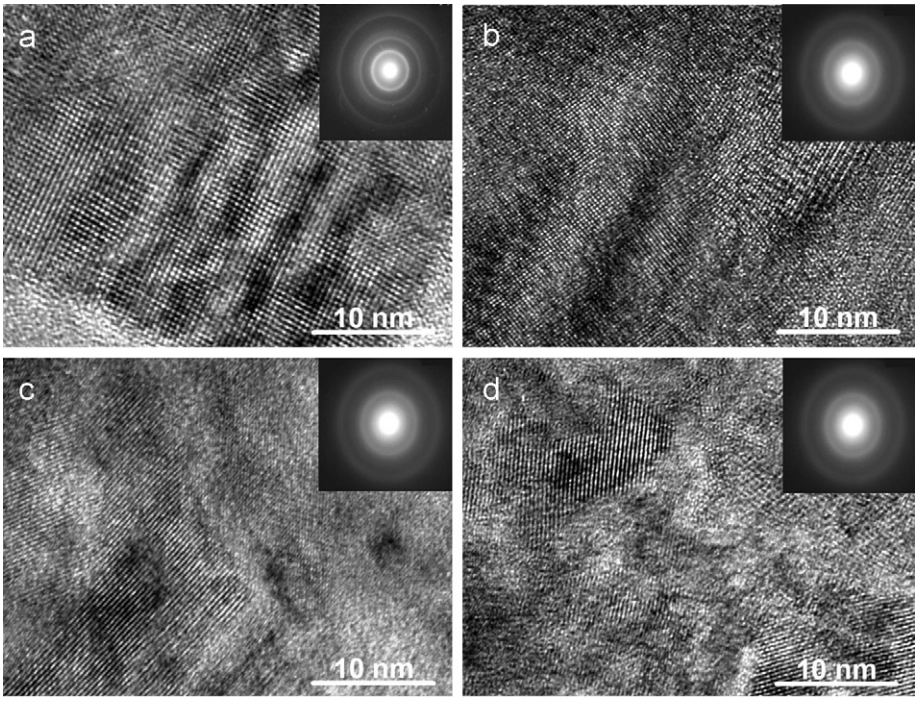

Fig. 3. HRTEM micrographs and ED patterns of the as-spun $Mn_{0.3}$ alloy: (a) 15 m/s, (b) 20 m/s, (c) 25 m/s, (d) 30 m/s.

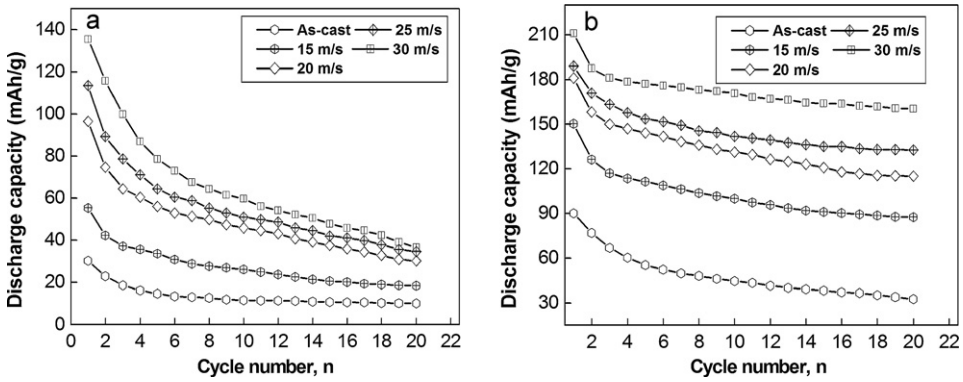

Fig. 4. Evolution of the discharge capacity of the alloys with the cycle number: (a) Mn_0 alloy, (b) $Mn_{0.3}$ alloy.

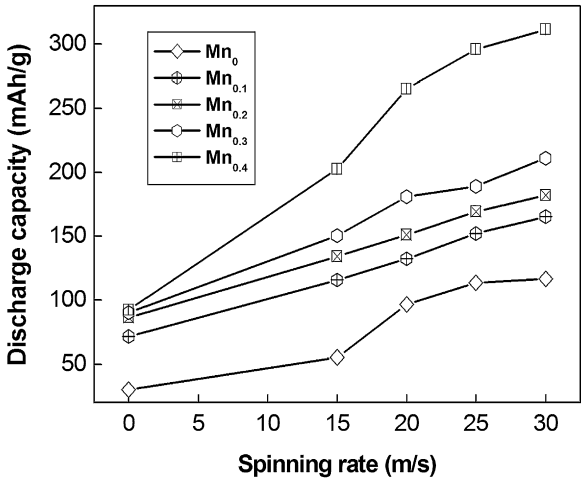

Fig. 5. Evolution of the maximum discharge capacity of the alloys with the spinning rate.

are directly proportional to the internal strain. Therefore, it is understandable that the introduction of defects, disordering and internal strain leads to an increasing discharge capacity.

3.2.2. Charging and discharging cycle stability

The cycle stability of the electrode alloy is a decisive factor of the life of the Ni-MH battery. The cycle stability of the alloy is symbolized by the capacity retaining rate (S_n), being defined as $S_n = C_n/C_{max} \times 100\%$, where C_{max} is the maximum discharge capacity and C_n is the discharge capacity at the nth charge–discharge cycle, respectively. The spinning rate dependence of the S_{20} ($n = 20$) values of the alloys is plotted in Fig. 6. Apparently, the melt spinning exerts different impact on the S_{20} values of the Mn-free and containing Mn alloys. With the increase in the spinning rate from 0 to 30 m/s, the S_{20} value falls from 33.5% to 30.4% for the Mn_0 alloy, whereas it mounts up from 36.2% to 76.0% for the $Mn_{0.3}$ alloy. In order to signally view the process of the capacity degradation of the alloy electrode, the evolution of the S_n values of the Mn_0 and $Mn_{0.3}$ alloys with the cycle number is shown in Fig. 7. A rough tendency shows that the as-cast and spun Mn_0 alloy exhibits the nearly same decay rates of the discharge capacities, whereas those

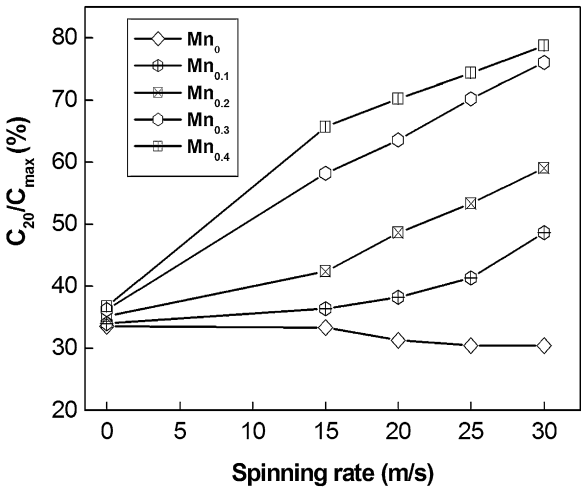

Fig. 6. Evolution of the capacity retaining rate (S_{20}) of the alloys with the spinning rate.

of the $Mn_{0.3}$ alloys evidently fall with rising spinning rate, suggesting that the melt spinning enhances the cycle stability of the $Mn_{0.3}$ alloy. It was well known that the severe corrosion of Mg in the alkaline KOH solution is the essential reason of leading to the capacity degradation of the Mg-based alloy electrodes. Especially, during the discharging process, the alloys are anodically polarized so that corrosion would be faster [2]. On the other hand, the metastable structures formed by melt spinning or ball milling tended to vanish during multiple charging/discharging cycles, which is an important factor for the capacity decay of the alloys [22]. The nanostructure exhibiting by the alloys resulting from melt spinning has been considered to be detrimental due to its corrosion in the electrolyte during cycling on account of the fact that the intercrystalline corrosion is facilitated by the nanostructure formation. This provides an illustration for the decline in the cyclic stability of the Mg–Ni system alloy caused by a higher spinning rate. The positive impact of Mn substitution on the cycle stability of the alloy is ascribed to following reasons. One is that the enlarged cell volume caused by Mn substitution decreased the ratios of expansion/contraction of the alloys in process of the hydrogen absorption/desorption, which means increasing the anti-pulverization capability of the alloy. On the other hand, the glass forming ability enhanced by Mn substitution is extremely important because an amorphous phase improves not only anti-pulverization ability but also anti-corrosion and anti-oxidation abilities of the alloy electrode in a corrosive electrolyte [23]. Additionally, the addition of third element significantly stabilizes the nanostructure of the as-spun alloy [14], reflecting an increase of the cycle stability of the alloy.

3.3. Hydrogen absorption and desorption kinetics

The hydriding process was carried out under 1.5 MPa hydrogen pressure (in fact, this is initial pressure of hydriding process) at 200 °C, and dehydriding process was carried out in a vacuum (1×10^{-4} MPa) at 200 °C, too. The hydrogen absorption kinetic curves of the Mn_0 and $Mn_{0.3}$ alloys are plotted in Fig. 8. It can be seen that hydriding kinetic curves of the as-spun Mn_0 and $Mn_{0.3}$ alloys show an initial fast hydrogen absorption stage after which the hydrogen content is saturated at longer hydrogenation time, indicating that the melt spinning improves the hydrogen absorption property of the alloys. Generally, the hydrogen absorption kinetics of the alloy is symbolized by hydrogen absorption saturation

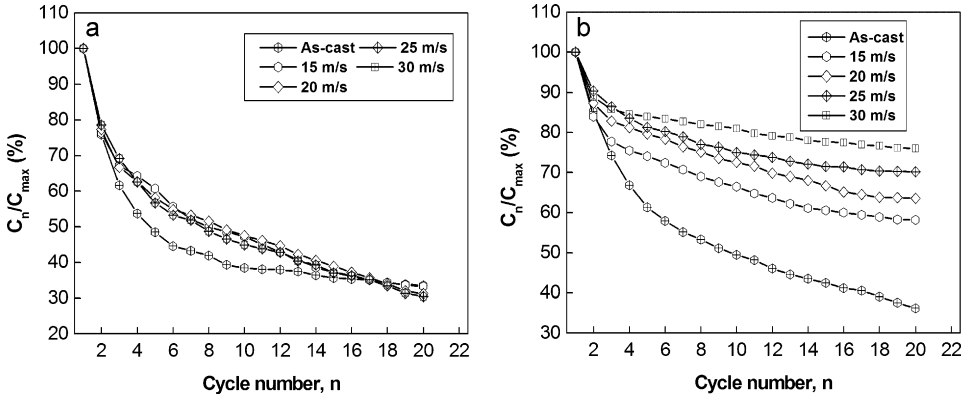

Fig. 7. Evolution of the capacity retaining rate of the alloys with cycle number: (a) Mn_0 alloy, (b) $Mn_{0.3}$ alloy.

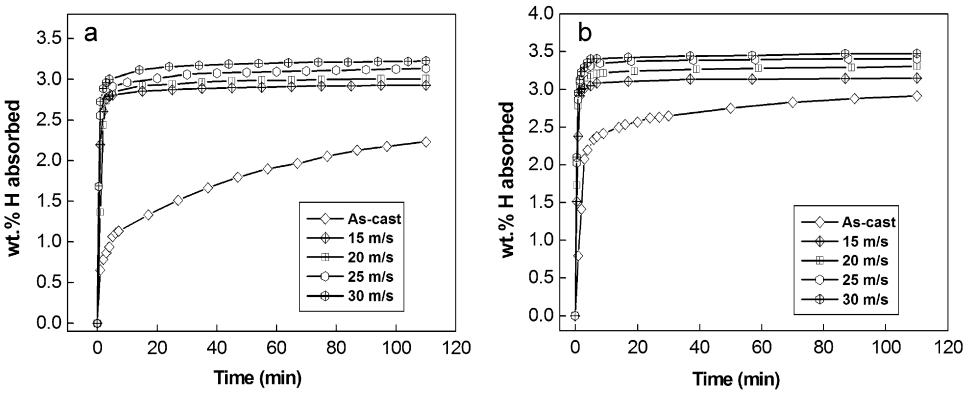

Fig. 8. Hydrogen absorption kinetic curves of the as-cast and spun alloys: (a) Mn_0 alloy, (b) $Mn_{0.3}$ alloy.

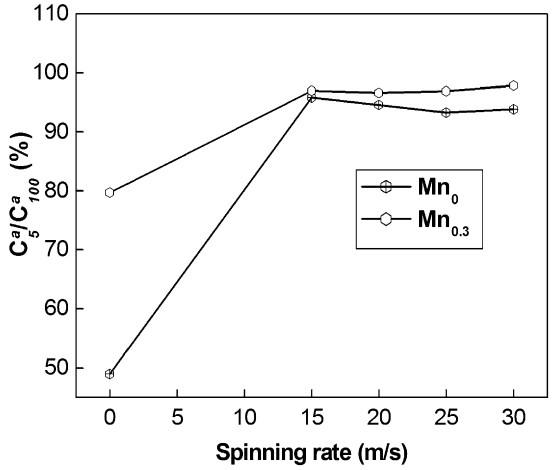

Fig. 9. Evolution of hydrogen absorption saturation ratio (R_5^a) of the alloys with spinning rate.

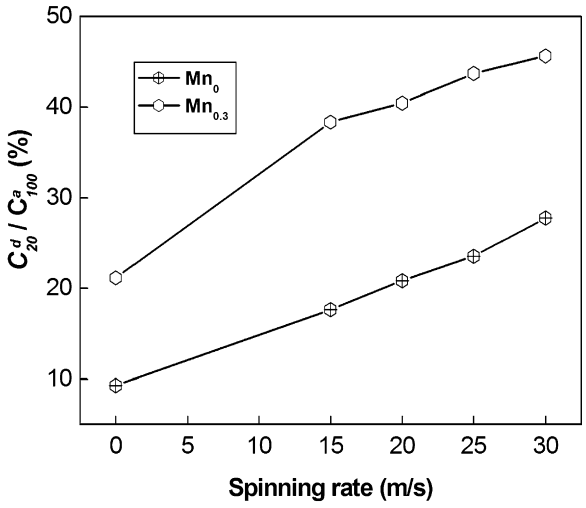

Fig. 11. Evolution of hydrogen desorption ratio (R_{20}^d) of the alloys with spinning rate.

ratio (R_t^a), being defined as $R_t^a = C_t^a/C_{100}^a \times 100\%$, where C_{100}^a is the hydrogen absorption capacity in 100 min and C_t^a is the hydrogen absorption capacity in the time of t min, respectively. Apparently, for a fixed time t, a larger saturation ratio R_t^a means better hydrogen absorption kinetics. The hydrogen absorption saturation ratio (R_5^a) ($t = 5$) of the alloys as a function of the spinning rate is presented in Fig. 9. The figure indicates that the melt spinning leads to a marked increase in the R_5^a values of the alloys. With the increase in the spinning rate from 0 to 30 m/s, R_5^a value grows from 49.01% to 93.86% for the Mn_0 alloy, and from 79.73% to 97.89% for the $Mn_{0.3}$ alloy. The hydrogenation kinetics and storage capacity of the as-spun nanocrystalline Mg_2Ni-type alloys studied are superior to those of conventional polycrystalline materials with similar composition. A similar result was reported by Spassov and Köster [24]. Orimo and Fujii [25] validated that the hydrides mainly exist in grain-boundary amorphous phase regions. The improved hydrogenation characteristics can be explained with the enhanced hydrogen diffusivity in the nanocrystalline microstructure as the nanocrystalline leads to an easier access of hydrogen to the nanograins, avoiding the long-range diffusion of hydrogen through an already formed hydride, which is often the slowest stage of absorption. It is known that the nanocrystalline microstructures can accommodate higher amounts of hydrogen than polycrystalline ones. The large number of interfaces and grain boundaries available in the nanocrystalline materials provide easy pathways for hydrogen diffusion and promote the absorption of hydrogen.

The hydrogen desorption kinetic curves of the as-cast and spun Mn_0 and $Mn_{0.3}$ alloys are illustrated in Fig. 10. An important feature of the dehydrogenation process in the alloys is very slow initial hydrogen desorption, followed by slack increase in the amount of hydrogen absorbed. Fig. 10 shows that the melt spinning markedly improves the hydrogen desorption capacity and kinetics of the Mn_0 and $Mn_{0.3}$ alloys. Similarly, the hydrogen desorption kinetics of the alloy is signified by hydrogen desorption ratio (R_t^d), being defined as $R_t^d = C_t^d/C_{100}^a \times 100\%$, where C_{100}^a is the hydrogen absorption capacity in 100 min and C_t^d is the hydrogen desorption capacity in the time of t min, respectively. It is reasonable to take the C_{100}^a value as the saturated hydrogen absorption capacity of the alloy because the experimental result indicates that the C_{100}^a value is more than 95% of the saturated hydrogen absorption capacity for all the alloys. The hydrogen desorption ratio (R_{20}^d) ($t = 20$) of the alloys as a function of the spinning rate is depicted in Fig. 11, indicating that the R_{20}^d values of the alloys increase with rising spinning rate. As the spinning rate grows from 0 to 30 m/s, the R_{20}^d value mounts up from 9.28% to 27.77% for the Mn_0 alloy, and from 21.16% to 45.62% for the $Mn_{0.3}$ alloy. Apparently, Mn substitution markedly enhances the hydrogen desorption kinetics of the alloys. The observed essential differences in the hydriding/dehydriding kinetics of the as-cast and spun alloys studied most probably have to be associated with their microstructure due to the different spinning rates. It was reported that the high surface to volume ratios, i.e. high specific surface area, and the presence of large number of grain boundaries in nanocrystalline and amorphous alloys enhance the kinetics of hydrogen absorption/desorption [15]. Two reasons are mostly responsible for the impact action of Mn substitution on the dehydriding

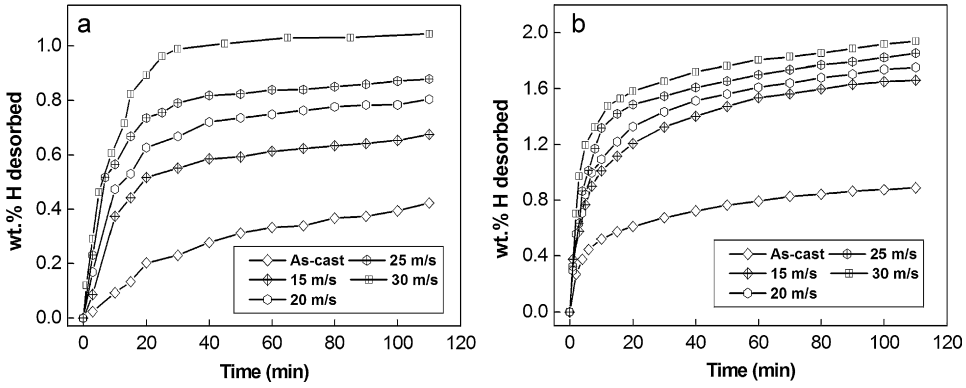

Fig. 10. Hydrogen desorption kinetic curves of the as-cast and spun alloys: (a) Mn_0 alloy, (b) $Mn_{0.3}$ alloy.

kinetics of the alloys. Firstly, the partial substitution of element Mn for Ni in Mg_2Ni compound decreases the stability of the hydride and makes the desorption reaction easier [26]. Secondly, the presence of secondary phase MnNi apparently has catalytic effects for the hydriding and dehydriding reactions of Mg and Mg-based alloys [12]. In multi-component Mg–Ni based hydrogen storage alloys surface segregation and formation of microcrack passages for H-diffusion improve the kinetics of hydriding/dehydriding.

4. Conclusions

1. The investigation on the structures of the as-cast and spun $Mg_2Ni_{1-x}Mn_x$ ($x = 0, 0.1, 0.2, 0.3, 0.4$) alloys shows that there is no amorphous phase in the as-spun Mn-free alloy, but the as-spun alloys containing Mn present an evident feature of the nanocrystalline embedded in the amorphous matrix. The amorphization degree of the alloys visibly increases with rising spinning rate.
2. Melt spinning considerably enhances not only the electrochemical discharge capacity of the alloys but also the electrochemical cycle stability of the alloys containing Mn. But it slightly impairs cycle stability of the Mn-free alloy, for which the different structure formed by the melt spinning is basically responsible.
3. Melt spinning significantly improves the hydriding and dehydriding properties of the alloys. Hydriding and dehydriding capacities and rates of the alloy markedly increase with rising spinning rate.

Acknowledgements

This work is supported by National Natural Science Foundations of China (50871050), Natural Science Foundation of Inner Mongolia, China (200711020703) and Higher Education Science Research Project of Inner Mongolia, China (NJzy08071).

References

[1] L. Schlapbach, A. Züttel, Nature 414 (2001) 353–358.
[2] M.V. Simičić, M. Zdujić, R. Dimitrijević, Lj. Nikolić-Bujanović, N.H. Popović, J. Power Sources 158 (2006) 730–734.
[3] L. Schlapbach, MRS Bull. 27 (2002) 675–676.
[4] A. Ebrahimi-Purkani, S.F. Kashani-Bozorg, J. Alloys Compd. 456 (2008) 211–215.
[5] P. Palade, S. Sartori, A. Maddalena, G. Principi, S. Lo Russo, M. Lazarescu, G. Schinteie, V. Kuncser, G. Filoti, J. Alloys Compd. 415 (2006) 170–176.
[6] D. Kyoi, T. Sakai, N. Kitamura, A. Ueda, S. Tanase, J. Alloys Compd. 463 (2008) 306–310.
[7] X.F. Liu, Y.F. Zhu, L.Q. Li, J. Alloys Compd. 455 (2008) 197–202.
[8] F.J. Liu, S. Suda, J. Alloys Compd. 231 (1995) 742–750.
[9] C.X. Shang, M. Bououdina, Y. Song, Z.X. Guo, Int. J. Hydrogen Energy 29 (2004) 73–80.
[10] B. Sakintuna, F. Lamari-Darkrim, M. Hirscher, Int. J. Hydrogen Energy 32 (2007) 1121–1140.
[11] G. Liang, J. Alloys Compd. 370 (2004) 123–128.
[12] M.Y. Song, S.N. Kwon, J.S. Bae, S.H. Hong, Int. J. Hydrogen Energy 33 (2008) 1711–1718.
[13] M. Savyak, S. Hirnyj, H.-D. Bauer, M. Uhlemann, J. Eckert, L. Schultz, A. Gebert, J. Alloys Compd. 364 (2004) 229–237.
[14] L.J. Huang, G.Y. Liang, Z.B. Sun, Y.F. Zhou, J. Alloys Compd. 432 (2007) 172–176.
[15] T. Spassov, U. Köster, J. Alloys Compd. 279 (1998) 279–286.
[16] L.J. Huang, G.Y. Liang, Z.B. Sun, D.C. Wu, J. Power Sources 160 (2006) 684–687.
[17] S.I. Yamaura, H.Y. Kim, H. Kimura, A. Inoue, Y. Arata, J. Alloys Compd. 339 (2002) 230–235.
[18] A. Inoue, T. Masumoto, Mater. Sci. Eng. A 173 (1993) 1–8.
[19] H.S. Chen, Acta Metall. 22 (12) (1974) 1505–1511.
[20] G. Friedlmeier, M. Arakawa, T. Hiraia, E. Akiba, J. Alloys Compd. 292 (1999) 107–117.
[21] H. Niu, D.O. Northwood, Int. J. Hydrogen Energy 27 (2002) 69–77.
[22] G.Y. Liang, D.C. Wu, L. Li, L.J. Huang, J. Power Sources 186 (2009) 528–531.
[23] Y.H. Zhang, B.W. Li, H.P. Ren, Y. Cai, X.P. Dong, X.L. Wang, Int. J. Hydrogen Energy 32 (2007) 4627–4634.
[24] T. Spassov, U. Köster, J. Alloys Compd. 287 (1999) 243–250.
[25] S. Orimo, H. Fujii, Appl. Phys. A 72 (2001) 167–186.
[26] J.H. Woo, K.S. Lee, J. Electrochem. Soc. 146 (1999) 819–823.